Microstructural Controls on Monosulfide Weathering and Heavy Metal Release (MIMOS)

Pollok K. (1)*, Harries D. (1), Hopf J. (1,2), Etzel K. (1), Chust T. (1), Hochella M.F., Jr. (3), Hellige K. (4), Peiffer S. (4), Langenhorst F. (1)

(1) Universität Bayreuth, Bayerisches Geoinstitut, D-95440 Bayreuth, kilian.pollok@uni-bayreuth.de

(2) Friedrich-Schiller-Universität Jena, Institut für Mikrobiologie, Neugasse 25, D-07743 Jena

(3) Center for NanoBioEarth, Department of Geosciences, Virginia Polytechnic Institute and State University, Blacksburg, Virginia, USA

(4) Universität Bayreuth, Lehrstuhl für Hydrologie, D-95440 Bayreuth

* Coordinator of the project

1. Introduction and summary

The iron monosulfides pyrrhotite ($Fe_{1-x}S$) and mackinawite (tetragonal FeS) are both environmentally important phases linking the iron and sulfide elemental cycle. This report summarizes studies that aim at understanding on the effect of microstructure, mineral chemistry and crystallography of these minerals on the reactivity (*Pollok et al., 2008*) and provides insights towards possible applications.

Pyrrhotite comes a close second after pyrite among the most abundant iron sulfides in crustal rocks and ore deposits including Ni-Cu, Pb-Zn, Au, and platinum-group elements (PGE). The weathering of pyrrhotites contributes to the release of iron and other metals as well as sulfate to surface waters as a part of the acid mine drainage problem. The relevance of this reaction lies in the high reactivity of pyrrhotite (20 to 100 times faster compared to the disulfide pyrite; *Nicholson & Scharer, 1994*) which limits the neutralization of produced sulfidic acid by silicate weathering reactions. Furthermore, many potentially important implications to the fields of geomagnetics, petrology, environmental mineralogy, and technical mineral processing are to be expected if detailed knowledge about structures and phase relations is available. Lately, the flotation behavior of pyrrhotite is attracting more attention as this mineral is an important host for Ni and PGEs (*Becker et al., 2010; Ekmekçi et al., 2010*).

In the first section the coupling between crystallographic structure and composition of pyrrhotite has been studied by the use of transmission electron microscopy (TEM) which has been used for the first time to directly visualize details of the (non-integral) stacking sequences using superstructure diffraction spots. The observations result in a new and versatile description of pyrrhotite superstructures which provide a basis to understand variation in physical properties and reactivity of pyrrhotites. In the second section the relevance of different superstructures in terms of reactivity is directly substantiated for the biologically-enhanced dissolution of a pyrrhotite intergrowth. The difference in dissolution rates betwee the intergrown phases is quantified by using topographic data produced by confocal microscopy providing a new view on the reactivity and weathering patterns of this mineral. The third part deals with the evolution of surface roughness for such reacted and heterogeneous surfaces. To extend our possibilities to generate meaningful data for reactive surface area and, hence, dissolution rates, a new program is introduced, which allows a non-biased statistical evaluation of surface roughness distributions. The concept presented here can be utilized for any kind of topographic data and might be well applicable to other areas of surface science.

Mackinawite is a metastable, nanoparticular phase that forms by precipitation from aqueous solutions at low temperatures. It is a major component of acid volatile sulfide (AVS) compounds, causing black-colored layers in recent anoxic sediments. Mackinawite is therefore an important precursor of sedimentary pyrite and can facilitate in-situ remediation of metals in connection with (biogenic) sulfate reduction in acidic pit lakes and sediments (*Bilek, 2006, Church et al. 2007*). It is known as an effective absorber due to its large specific surface area (*Ohfuji & Rickard, 2006*) but detailed reaction mechanisms important to biogeochemistry are still missing.

The last section provides experimental evidence for the formation mechanisms of sedimentary sulfides via mackinawite under anoxic conditions. The results highlight the importance of iron hydroxide surfaces as the locations of electron transfer for mackinawite formation, but also show the spatial decoupling to pyrite formation. In conclusion, the study provides fundamental data that enables to model basic reactions at geochemical interfaces.

2. Towards a new structural model for NC-pyrrhotites: Structural and chemical characterization of selected samples by electron microscopy

The physical properties of a mineral and the reactivity of a mineral surface are determined by its chemical composition and internal atomic structure. In this respect, non-stoichiometric pyrrhotite is a striking phase because its structure and the physical (e.g. magnetic) properties change dramatically within a small compositional range. A detailed knowledge about the composition-structure relationship as well as the structure-property relationship is needed to gain a fundamental understanding of this environmentally and technically important mineral.

Pyrrhotite has a NiAs-derivative structure that contains sequences of hexagonal close-packed S atom layers stacked in alternation with layers of Fe atoms in octahedral coordination. Non-stoichiometric compositions arise from the presence of vacancies within Fe layers and span the range in-between ~47 to 50 at% Fe (Fe_7S_8 to FeS), whereas most structural complexity occurs in the narrow compositional range between 47 to 48 at% Fe. At temperatures below 300 °C various superstructures are observed in this range due to vacancy ordering among and within Fe layers, resulting in a rather complicated subsolidus phase diagram (e.g., *Nakazawa & Morimoto, 1970*).

Based on a NiAs-type structure of FeS, the well understood monoclinic 4C structure is derived by removing 1/4 of Fe atoms from every second Fe layer, leading to the composition Fe_7S_8. Four vacancy layers are mutually discernible in the stacked arrangement and the resulting sequence of partially vacant (V) and filled (F) Fe layers is $V_AFV_BFV_CFV_DF$. The spacing between V layers of the same type is strictly four times the c-axis repeat of the NiAs substructure (or eight Fe layers).

Structural descriptions of integral NC-pyrrhotite structures can be roughly divided into two approaches using either discrete (0 or 1) or partial Fe site occupancies. The former relates to an idealized extension of the 4C stacking scheme by introducing additional F layers, which increases both the periodicities of the superstructures as well as the Fe/S ratios, while the latter proposes in addition to extended layer stacking a considerable atomic scale disorder of Fe vacancies.

Yamamoto & Nakazawa (1982) developed a superstructure description for an N_c = 5.54 pyrrhotite based on a continuous modulation of (partial) Fe site occupancies. In this model of an aperiodic crystal structure the probability of finding a Fe atom at a given lattice site is governed by a continuous, sinusoid-like modulation function embedded in a four-dimensional superspace formalism. Aperiodicity results from the occupation modulation being incommensurately related to the substructure periodicity. Based on this work *Izaola et al.* (2007) introduced a generalized superspace approach by replacing the continuous occupancy modulation with a step-like function governing discrete site occupancies. By virtue of a »closeness« condition, the model strictly obeys the

sequence of ABCD layering as well as the rule that two V layers must not follow consecutively without an interjacent F layer, resulting in the fixed relation $1/N_c = 2x$ between superstructure N_c value and composition expressed as x in $Fe_{1-x}S$.

A primary motivation for this study was that the reported electron diffraction pattern of non-integral NC-pyrrhotites strongly resemble those seen in certain translation interface modulated binary alloys such as $Au_{3+x}Zn_{1-x}$ (*Amelinckx & Van Dyck, 1992*). In these alloy systems integral superstructures arise in stoichiometric compounds as Au_3Zn from ordering atoms on certain sites of the fcc lattice. Non-stoichiometric compositions and further superstructures are related to variably ordered, non-conservative (»composition-changing«) antiphase boundaries (APBs) of these simple superstructures. Such translation interface modulation (TIM) is characterized by replacement (or splitting) of the simple superstructure diffractions spots (e.g., those of 4C-pyrrhotite) with arrays of satellite reflections – as seen in NC-pyrrhotites.

2.1. Samples and experimental methods

In this study, two natural pyrrhotite samples from geologically different locations were characterized in detail by electron microscopy. Samples were obtained from the Sta. Eulalia mining district in Chihuahua, Mexico (EUL) and from the Nyseter mining area near Grua, Norway (NYS). Ar-ion thinning for transmission electron microscopy (TEM) was carried out using liquid nitrogen cooling or a low angle thinning system. In order to check for preparation artefacts, powdered and ultramicrotomed samples were prepared as well, but no systematic differences in SAED pattern could be detected. N_c values were obtained from selected area electron diffraction (SAED) patterns with typical uncertainties of ±0.01 (2s). TEM superstructure dark-field imaging (SDF) was accomplished by placing an objective aperture of 2.3 nm^{-1} diameter on strong satellite reflections.

2.2. Results - Electron microprobe analysis (EMPA)

Back scatter electron (BSE) imaging of EUL and NYS shows abundant exsolution lamellae in both samples. In sections the lamellae form two sets of lens shaped or sigmoidal bodies inclined towards the [001] direction of host pyrrhotite. Lamellae typically measure <200 µm in length and up to 30 µm in width and are darker in BSE images (Fig. 1a). Quantitative analyses show the lamellae to have compositions near $Fe_{0.875}S$ (or Fe_7S_8) indicative of 4C-pyrrhotite, while the host pyrrhotites' Fe contents are slightly below $Fe_{0.900}S$ (or Fe_9S_{10}) as indicated by x values of 0.106±0.001 (EUL) and 0.102±0.001 (NYS). Contrary to the EUL sample NYS shows a small Ni content of 0.05 to 0.11 wt%. Exsolution of 4C-pyrrhotite from NC-pyrrhotite appears to be quite abundant in nature and is well documented by petrographic methods.

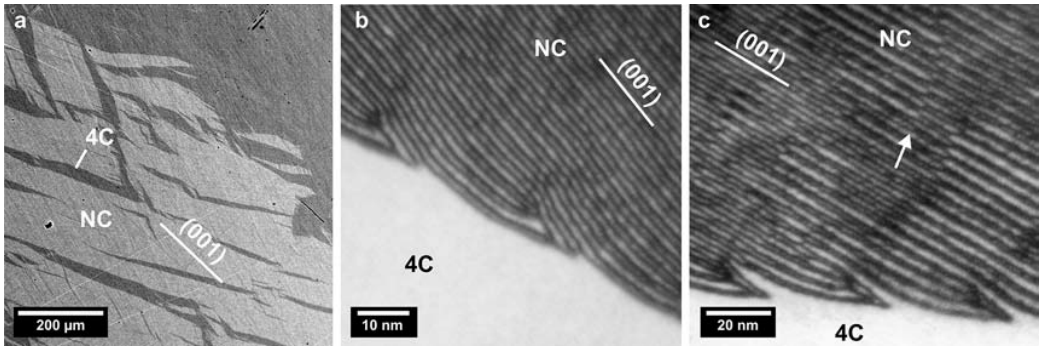

Figure 1: (a) BSE image of 4C/NC intergrowths in sample EUL. (b) TEM-SDF image of the 4C/NC interface in EUL. APBs terminate in eight-fold node structures. (c) TEM-SDF image of the 4C/NC interface in sample NYS. Nearly identical node structures occur at the boundary but additionally changes in APB configurations (arrow) in the NC phase can be seen

2.3. Results - TEM-SAED

The indexing of superstructure satellite reflections is done by applying a (3+1)-dimensional (hklm) scheme analogous to the one adopted by *Yamamoto & Nakazawa* (1982) and commonly used for the description of one-dimensionally modulated structures (Fig. 2). A diffraction vector **g** is thus:

$$\mathbf{g} = h\,\mathbf{a^*} + k\,\mathbf{b^*} + l\,\mathbf{c^*} + m\,\mathbf{q}$$

m is the satellite order of a superstructure reflection and **q** is the modulation vector relating each satellite to a (*hkl*) substructure reflection. **q** is generally parallel or subparallel to **c***. The N_c value of a superstructure is obtained as the length ratio **c***/**q** with c* referring to the NiAs-type subcell ($c^* \approx 1.72$ nm^{-1}). For the EUL and NYS samples coincident N_c values of 4.81-4.87 and 4.78-4.96, respectively, have been obtained. In general, the Nc values compare well to the x values obtained from EMPA assuming the relation $1/N_c = 2x$.

Based on the hypothesis of an APB modulation, the splitting of reflections in SAED patterns obtained from zone axes perpendicular to c allows to calculate average spacings and displacement vectors of APBs (*Amelinckx & Van Dyck, 1992*). The geometrical evaluation of pattern obtained from EUL and NYS suggest spacings of 1.58 to 1.74 nm and a displacement vector $\mathbf{R} = 1/8[001]_{4H}$ (the 4H indexing refers to a hexagonal cell in which the NiAs a and c dimensions are doubled and quadrupled, respectively).

2.4. Results - TEM-SDF

In order to obtain TEM-SDF images from electron beams diffracted by the superstructure, it was found to be most effective to place the objective aperture on the (0004) and (008-4) satellite reflections accessed from near the $[210]_{4H}$ zone axis. The sample foil was tilted such that in the ideal case only diffracted beams in the (00l*m*) reciprocal lattice row were excited. In the NC portions of both the EUL and NYS samples, SDF images reveal dense arrays of dark stripes being aligned parallel to the (001) planes and solely visible in dark-field images using strong superstructure reflections. In EUL the stripes appear more ordered and show less wiggles and irregularities compared to NYS, which displays some weak diffuse diffraction in the area from which the images were obtained. Further, in NYS the configuration of stripes appears to change along certain domain boundaries where the thin stripes, as seen in EUL, change into thicker stripes. The latter dominate the NYS sample and are likely doublets of two stripes being too close to be resolved under the SDF imaging conditions. The average spacing of stripes in EUL is 1.63±0.05 nm and the observed (half-)width of a single stripe is approx. 0.80 nm. Assuming the thick stripes in NYS to be non-resolvable doublets, the average spacing between individual stripes is 1.94±0.10 nm.

The average distance for EUL compares very well with the expected APB spacing as obtained from the SAED pattern geometries and we therefore interpret the dark stripes to be APBs. Based on contrast in dark-field images we can exclude them to be stacking faults or twin boundaries, as the former would be seen with substructure reflections as well and the latter would show intensity differences of domains on either site of the boundary. The larger average spacing in NYS, despite very similar N_c values, is likely due to the higher disorder with larger and more irregular spacings between stripes which bias the mean distance to higher values. The average of 1.94 nm corresponds to an N_c value of approx. 4.7, which is compatible with diffuse satellite reflections seen in some SAED patterns.

Most striking features in SDF images of EUL and NYS are the phase boundaries between 4C- and NC-pyrrhotite where the stripes form complicated but remarkably similar node structures in which the stripes terminate. When the phase interface is oriented mostly parallel to the stripes, no nodes occur directly at the interface, but occasionally appear nearby within the NC phase, often associated with crystallographic edge dislocations having the Burgers vector **b** = [001] of the NiAs cell. In all cases of node structures we observed eight stripes to terminate in a single node.

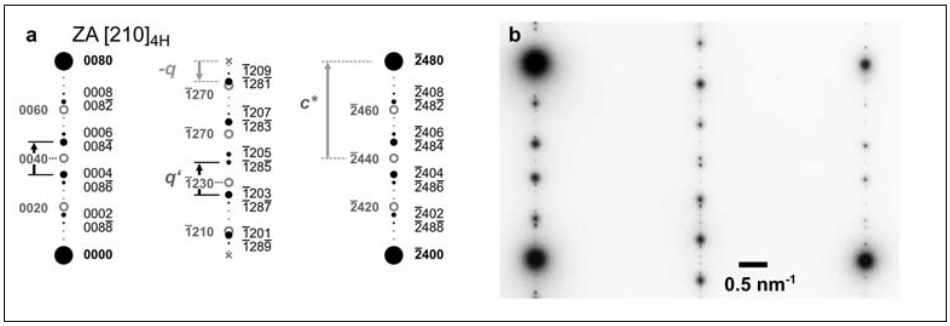

Figure 2: Diffraction patterns of non-integral NC-pyrrhotite. (a) Schematic representation of zone axis [210] for N_c = 4.85. Grey open circles/indices represent 4C reflections, crosses mark the (generally absent) 4C reflections used for superstructure indexing. (b) Experimental SAED pattern of NYS with N_c = 4.84±0.01

The behavior of stripes in the observed node structures and adjacent 4C-pyrrhotite strongly endorses our interpretation of them being non-conservative APBs of the 4C structure. Their orientation is fully compatible with the inferred displacement vector **R** = $1/8[001]_{4H}$ which creates double layers of completely filled Fe positions as opposed to single layers being present in the 4C structure. The eight-fold nodes facilitate the reconstruction of the 4C phases from the APB modulated NC phase and directly support the proposed displacement vector $1/8[001]_{4H}$ as its eight-fold multiple will be the c dimension of the hexagonal 4C unit cell (see discussion section). Apparently the highly similar node configurations represent a self-organization towards an energetically optimal phase interface.

2.5. Discussion

Our TEM observations provide compelling evidence that the structural diversity of non-integral NC-pyrrhotites can be explained in terms of a TIM structure model. The translation interfaces are APBs based on the Fe sublattice of 4C-pyrrhotite. This model bears resemblance to previously suggested »out-of-step« and anti-phase defect models (*Pierce & Buseck, 1974*) but is more precise on the actual nature of the involved translation interfaces. On the other hand, the superspace approach of *Izaola et al. (2007)* is fully compatible with our TIM model. In essence, this superspace model produces discretely modulated superstructures by inserting additional F layers into the basic 4C layer sequence, producing either periodic or aperiodic (but uniform) stacking sequences parallel to (001). Because the so produced double F layers carry an Fe excess, the resulting phases will have higher Fe/S ratios than 4C-pyrrhotite and follow strictly the relation $1/N_c = 2x$ as spacings between double layers are evenly distributed.

For a structure with N_c = 4.8, which is a simple representation for the host NC-pyrrhotite in our EUL and NYS samples, it is possible to derive two well ordered stacking schemes: $(DSSDS)_4$ and $(DDSSS)_4$, where D represents double F layers and S single F layers, intercalated with the four vacancy bearing layers. The $(DSSDS)_4$ sequence can be derived via the superspace model of *Izaola et al.* (2007) and is uniform, while the $(DDSSS)_4$ sequence cannot be obtained from the model and has less equally spaced D layers, leading to slightly less order while maintaining the same average vacancy-vacancy distance.

The observed D layer or APB arrangements in EUL are alike the well ordered $(DSSDS)_4$ sequence, while in NYS domains relating to both stacking schemes coexist as indicated by the changes in stripe configuration. Here the domains containing the thicker, non-resolvable stripes may correspond to the $(DDSSS)_4$ stakking in which the closest spacing between D layers or APBs is approx. 0.86 nm and thus more or less equal to the half-width of a single stripe as observed in EUL. The average ~1.72 nm D layer spacing of the idealized $(DSSDS)_4$ sequence compares well with the average stripe and APB spacings in EUL as obtained from

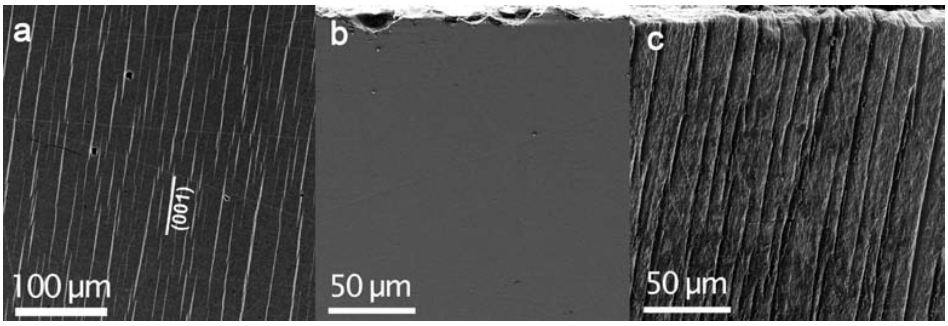

Figure 3: a) BSE image of the TYS sample. Bright lamellae contain 2 wt% more iron than the matrix. b) SE image of the surface of the abiotically reacted pyrrhotite cubes after 40 days which shows almost no dissolution. c) SE image of the pyrrhotite surface reacted with *A. ferrooxidans* after 40 days. Deep trenches formed at the position of the stoichiometric FeS lamellae

SDF images and SAED patterns, respectively, and consistently reproduces the observed slightly non-equal spacings in the bulk NC phase. It appears reasonable to assume that in case of NYS the energetic difference between both arrangements of D layers in the $(DSSDS)_4$ and $(DDSSS)_4$ stacking variants are very small and either the structure is observed on a transition to a more ordered state as in EUL or the elevated Ni content exerts some control on vacancy arrangements.

So far the discussion focused on an idealized layer stacking involving parallel layer arrangements. SDF images clearly shows that this ideal situation is virtually never fulfilled in the studied samples as stripes and therefore APBs are slightly wavy, corrugated and often non-parallel. Changes in stacking schemes at given Nc values as well as disorder introduced by bent APBs will not produce strong effects in SAED patterns. For the $(DSSDS)_4$ and $(DDSSS)_4$ stakking schemes the diffraction pattern geometries will be the same with only moderate differences in spot intensities, likely being hidden by dynamical diffraction effects. Increasing mesoscale disorder of APBs will first lead to vanishing higher order satellite reflections and gradually lead to streaky diffraction along the **c*** direction when a quasi-periodicity is no longer maintained. While a D layer in the ideal layer model is always an APB of the Fe sublattice the converse is not strictly true as isolated APBs are capable of moving more or less freely through the crystal and can have even in the confinement of a modulated structure a much more dynamical behavior as represented by a static layer model. Therefore, describing the layer stacking as a TIM structure of densely arranged APBs offers much better prospects of understanding the behavior and properties of non-integral NC-pyrrhotites.

The need of a more dynamical model clearly becomes apparent when trying to understand the node structures observed at NC/4C phase interfaces. The termination of eight stripes equivalent to eight APBs in a single node is necessary to reconstruct the 4C structure from an NC structure with well ordered V layer stakking. Because the stacking of V layers on the left side strictly obeys the ABCD sequence, the termination creates a sequence fault where two VF layers follow on each other. Consequently, two APBs have to terminate either at a perfect dislocation with $\mathbf{b} = [001]_{NiAs} = 1/4[001]_{4H}$, which removes a pair of VF layers, or 4 pairs of APBs have to terminate close-by such that the eight $1/8[001]_{4H}$ displacement vectors add up to the 4C lattice repeat. Both variants and combinations thereof are seen in our samples and we suggest that the observed node configurations facilitate an energetically most favorable state when there are no or few dislocations involved.

Based on the TIM model we suggest that there is no significant difference between integral and non-integral pyrrhotites and both types

can be understood as part of a continuum of structures in-between Fe_7S_8 and (at least) $Fe_{11}S_{12}$, in which variable Fe contents are governed by changes in densities and ordering states of APBs. Based on the presented data and preliminary data on other natural pyrrhotite samples we currently do not see evidence for preferred stability of integral NC-pyrrhotites in exsolution association with 4C-pyrrhotite, but the true phase relations may be obscured by slow diffusion kinetics below 220 °C, where NC-pyrrhotites first appear (*Nakazawa & Morimoto, 1970*). However, the very sharp compositional gradients at the 4C/NC interfaces in our EUL and NYS samples point to well equilibrated assemblages. Therefore, the association of $N_c \approx 4.85$ pyrrhotite with exsolved 4C-pyrrhotite in two of our samples, as well as the coexistence of $N_c = 4.88$ pyrrhotite and 4C-pyrrhotite observed by *Morimoto et al.* (1975), points to a favored stability of NC-pyrrhotites within the range of $N_c = 4.8$ to 4.9 – at least with regards to typical temperatures of the uppermost crust, where the samples resided for geological timescales.

The insight into complexity in the bulk structure and the applied TIM model can lead to a better understanding of physical properties and the reactivity of surfaces. Due to the rather two dimensional, layer-like structure of pyrrhotites one clear expectation is a pronounced anisotropy of surface properties. Preliminary experimental results indicate that reaction speeds on basal (001) faces are considerably different than on prismatic (*hk0*) surfaces. Owing to pyrrhotite's excessively variable magnetic and physicochemical properties and widespread occurrence in rocks and ore deposits, many potentially important implications to the fields of geomagnetics, petrology, environmental mineralogy, and technical mineral processing (e.g. pyrrhotite flotation) are to be expected when the presented detailed characterization of structures and phase relations is applied.

3. Structural controls on the alteration of pyrrhotite by Acidithiobacillus ferrooxidans under acidic conditons

Based on the detailed characterization procedures described above, a well-directed study on the reactivity of pyrrhotite intergrowth in experiments with acidophilic microorganisms was conducted. Acidophilic microorganisms play a dominant role in acid mine drainage (AMD) and for the metal recovery from low-grade ores by bioleaching applications. A number of studies focused on the reaction paths of chemical and biological metal sulfide oxidation (*Rawlings, 2002; Schippers, 2004*). However, experimental studies on the biologically-enhanced pyrrhotite oxidation are still scarce (see *Belzile et al.* 2004 for review) or focus on bioleaching applications of low grade ores (*Ke & Li, 2006; Jiang et al., 2007*), but clearly indicate the catalytic effect of microorgansms without reporting a reliable characterization of the starting material and dissolution rates. *Schippers et al*. (2007) provides a potential pyrrhotite oxidation rate measured in a mine tailing using microcalorimetry, which suggests that natural rates can exceed laboratory rates by up to 4 orders of magnitude. Beside the enhancing effect of microbial consortia, pyrrhotite dissolution may be also influenced by the reactivity and intergrowth texture of different superstructures. *Janzen et al.* (2000) studied a number of pyrrhotite samples from different localities and determined the relative proportions of so-called monoclinic (mainly 4C) and hexagonal (NC) pyrrhotite. No systematic trend in dissolution rates were found, however, information about the intergrowth texture is missing for these samples.

Acidithiobacillus ferrooxidans, an acidophilic proteobacteria that catalyses the oxidation of ferrous iron, elemental sulfur and reduced sulfur compounds is by far the best characterized bioleaching microorganism and has been used in the presented study. Cells of *A. ferrooxidans* produce an exopolysaccharide (EPS) layer to attach to the sulfide mineral surface (*Gehrke et al., 1998*) and this attachment is viewed as a process by which the bacterial membrane components interact directly with metal and

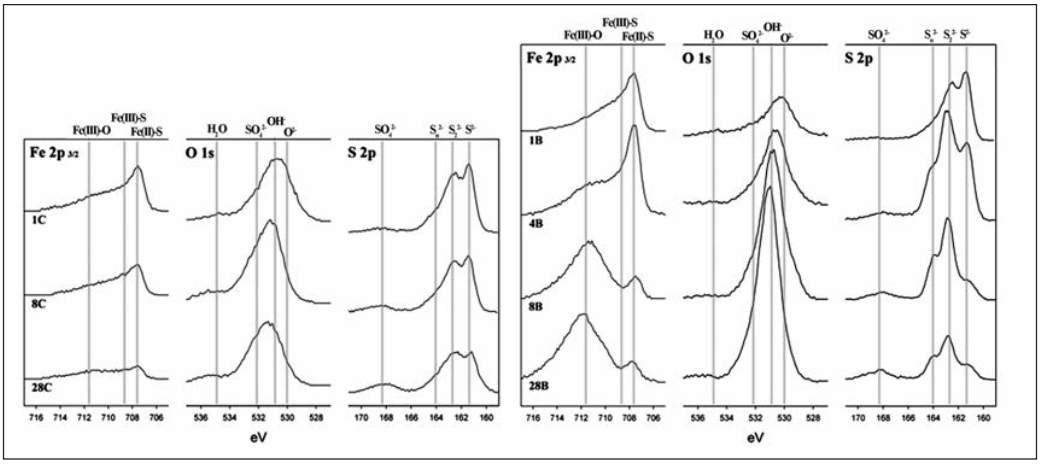

Figure 4: Overlays of the Fe $2p_{3/2}$, O 1*s* and S *2p* narrow region scans of pyrrhotite surfaces abiotic control (left) and biotic (right) experiments. Labels denote the duration of the experiments

sulfur of the mineral by an enzymatic type of mechanism (*Sand et al. 1995*).

In this study X-ray photoelectron spectroscopy (XPS), scanning electron microscopy (SEM), and confocal microscopy have been used to trace the chemical and morphological changes at the surface of a well characterized pyrrhotite sample. Surface topography has employed to quantify a differential dissolution rate between intergrown pyrrhotites.

3.1. Samples and experimental methods

A pyrrhotite from Tysfjord region, Norway (TYS) was used in this study. The TYS sample shows a dense population of 1-3 µm wide exsolution lamellae with a common orientation parallel to (001). They appear brighter in BSE images compared to the matrix indicating a higher Fe/S ratio (Fig. 3a). Quantitative analyses place them close to stoichiometric FeS (troilite). The matrix pyrrhotite of the TYS sample has a composition close to $Fe_{0.900}S$ (or Fe_9S_{10}) with x values of 0.096±0.001 and thus, the lamellae contain about 2 wt% more iron then the matrix.

Polished cubes (3x3x3 mm) of TYS pyrrhotite were dissolved in presence of *Acidithiobacillus ferrooxidans* at pH 2 over 40 days with an abiotic control in parallel. *A. ferrooxidans* ATCC 19859, obtained from the American Type Culture Collection (ATCC, Manassas, VA), was routinely cultivated as a pre-culture in ATCC medium 2039 at 28°C for five days on a rotary shaker (300 rpm). For the inoculation of the experiments 10 µl pre-culture (approx. 2×10^3 cells/ml) was directly used. Cultures for the experiments were grown in 50 ml mineral salt solution with 0.4 g each of $(NH_4)_2SO_4$, K_2HPO_4, and $MgSO_4\times7H_2O$ per liter. Cubes were removed from the batch experiments after 1, 4, 7, 14, 17, 21, 28 and 40 days, respectively.

XPS was performed on a PHI Quantera SXM-03 Scanning XPS Microprobe using an Al Kα X-ray source with a highly focused beam (<9 microns). High resolution scans of the Fe 2p, S 2p, and O 1s peaks were used to determine the bond and valence state information. XPS reference binding energies for pyrrhotite provided by *Legrand et al.* (2005) were used to assign and fit the spectra.

The topography of selected surfaces was measured by the confocal 3D microscopy system µsurf custom (Nanofocus AG, Oberhausen). It consist of a monochromatic LED light source (λ = 505 nm), a helically-shaped arrangement of pinholes (Nipkow-Disk), a stage with piezo module for z movement and a megapixel CCD camera. The objective used (numerical aperture 0.9) provides 160 µm x 160 µm field of view with a resolution of 10 nm in z and about 500 nm in x/y.

3.2. Results

A. ferrooxidans develops a visible biofilm on

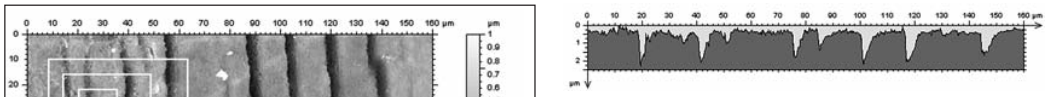

Figure 5: Surface of the TYS sample after biologically-enhanced dissolution measured for 28 days measured by confocal microscopy. The height of the matrix NC-pyrrhotite (~0.5 µm) was used as reference height to determine the differential dissolution rate from the dissolved volume of the 2C-lamellae. The squares illustrate the principle of roughness parameter calculation as function of sampling size performed with ROUGHNECK.
The upper profile clearly shows the non-symmetrical shape of the trenches which is explained by the inclined intersection of the lamellae with the surface

the pyrrhotite cubes after approximately 5 days of incubation. After 9 days the whitish biofilm covered the entire pyrrhotite cubes and grew slowly until the experiment was finally stopped at 40 days. After removing the biofilm by a washing procedure the color has changed to dark blue/black and the reflectivity from shiny to matt. In contrast, the control pyrrhotite cubes (abiotic) were still shiny golden in all experiments with only minor changes in reflectivity. XPS analyses (Fig. 4) reveal a significantly more oxidized surface in the biotic experiment with a clear shift from Fe(II)-S to Fe(III)-O bonding. Compared to the control experiment, the surface is more hydroxylated and shows even traces of sulfate. SEM images (Fig. 3) of the pyrrhotite surface exposed to A. ferrooxidans reveal long and deep trenches which start to develop already after 4 days of experiment. The position of the trenches is identical to the troilite lamellae indicating that the reactivity of the lamellae is significantly higher than the surrounding NC-pyrrhotite. Trenches reach depths of about 2 µm and a width of 3 µm as determined by confocal microscopy measurements after 28 days (Fig. 5). Height profiles suggest that the lamellae are inclined to the dissolving surfaces which lead to the nonsymmetrical shape of trenches. Although information of the original surface height is missing, the 3D topographic data can provide a differential dissolution rate of the 2C-pyrrhotite compared to the NC-pyrrhotite by using the matrix surface as a reference height. Five topographic images taken from surfaces after 21 and 28 days resulted in a differential dissolution rate of $8.8\pm1.2\times10^{-9}$ and $1.2\pm0.3\times10^{-8}$ mol $m^{-2}s^{-1}$, respectively.

3.3. Discussion

The dissolution experiments clearly show the catalyzing effect of microorganisms at conditions that are unfavorable for chemical dissolution. The XPS data indicates a fast and extensive oxidation of the biologically altered surface with dominating of Fe(III)-O bonds as well as some sulfate which points to the formation of a iron hydroxide layer (possibly FeOOH). However, this does not result in a passivation of the surface as indicated by a continuous deepening of the 2C lamellae which possible can be explained by the presence of EPS and a regeneration of ferric iron by the bacteria. For the first time, the clear difference in reactivity between two pyrrhotite superstructure (2C and NC) has been shown by the presented experiments. A direct and an indirect mechanism for biologically-enhanced dissolution have been proposed in the literature. For the direct mechanism, bacteria are attached to the surface surrounded by EPS which provides complexed ferric iron (*Rodriguez-Leiva & Tributsch, 1988*). The indirect mechanism interprets dissolution as an inorganic process where non-attached bacteria only maintain a certain ferric iron concentration which accelerates the dissolution (*Rodriguez et al., 2003*). Whether the difference in dissolution rate is facilitated by a preferred attachment of bacteria due to the different iron content or are caused by diffe-

rences in reactivity of troilite and NC-pyrrhotite alone is not yet been conclusively evaluated and will be subject of further activity. In any case, the lamellar structure of the trenches can not be interpreted as a primary microbial biosignatures because it is originally caused by the exsolution process during equilibration of the pyrrhotite sample and acts like a template during dissolution.

In any case, the differential dissolution rate is already higher than all reported abiotic dissolution rates and highlights the significance of the structural variability and intergrowth texture. When we combine the differential dissolution rate with the only available biotic dissolution rate for pyrrhotite under acidic conditions (8×10^{-9} mol $m^{-2}s^{-1}$) reported in *Belzile et al.* (2004), the resulting net dissolution rate is about one order of magnitude higher than reported rates in the absence of additional ferrous Fe. Further accelerating factors towards the observed rates include the combined effect of bacterial consortia (combinations of iron- and sulfur-oxidizer) as well as the increase of reactive surface area by the deepening of the trenches.

4. From surface morphology to rates: An automated routine to evaluate converged roughness parameters of heterogeneous surfaces

An increase of surface roughness during biologically-enhanced dissolution of pyrrhotite which, in turn, affects the dissolution rate was caused by both the microbial activity and the sample heterogeneity. Two components contribute to the surface roughness evolution of the TYS sample, namely, the alteration of the NC matrix and the deepening of trenches at the 2C lamellae. The high differential dissolution rate may be at least partly explained by increasing surface area. For the presented surfaces (Fig. 5) we are therefore interested in the evolution of surface roughness for the matrix, the lamellae and the combined surface of the biologically dissolved pyrrhotite surface, respectively.

In geosciences, rates are usually determined from dissolution studies (either flow through or batch experiments) using a size fraction of ground and sieved starting material by measuring the change in fluid chemistry as a function of time. The surface area of the starting material is commonly determined by the BET method and used as a constant to normalize rates. Recently, topographic methods have been introduced to directly measure sulfide dissolution rates and surface roughness (*Asta et al., 2008*) and offer new insides into the reaction mechanisms and surface reactivity. Furthermore, it allows a systematic determination of surface roughness parameters.

As statistical quantities roughness parameters are strongly dependent on the field of view of the used technique or the sampling size. The concept of »converged roughness parameter« (*Fischer & Lüttge, 2007*) was shown to be very useful to characterize certain surface building blocks by employing recurrent (squared) bisections of the measuring field with an edge length of a. A surface parameter is defined as converged when a flat slope is found in the convergence graph (roughness parameter versus edge length a). Converged parameters intrinsically depend on the choice of »representative« areas for their analysis. Furthermore, artificial measuring points may lead to an overestimation of roughness parameters. Here, we present the newly developed program ROUGHNECK, which calculates a number of surface roughness parameters from topographic data as function of sampling size allowing to analyze and visualize roughness parameter distributions.

4.1. The program ROUGHNECK

The program ROUGHNECK utilizes the common Surface Data Format (SDF) (*Blunt & Stout, 2001*) as input and output file format and is a stand-alone application that can be used on Windows and Linux systems. Our input files produced by confocal microscopy consist of 984x984 points representing a 160x160 µm field of view. For this study a quality criteria of a minimum of 99% of measured points was used for the topographic data. The residual non-measured points were linearly interpolated. The following 3D roughness parameters are implemented so far: the roughness average S_a, the root-mean-square roughness S_q, the

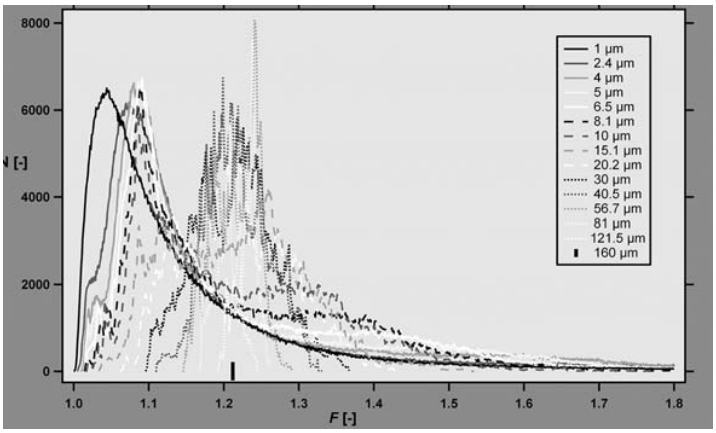

Figure 6: *F* value distributions for various squared sampling areas with a given edge length. With increasing sampling size the maximum of the curves is shifted to higher *F* values. However, the transition from low values around 1.05-1.1 to values around 1.2 is clearly visible and used in the convergence graph (Fig. 7a). For some curves (e.g. *a* = 4 µm) up to 3 maxima can be located indicating the heterogeneity of surface components

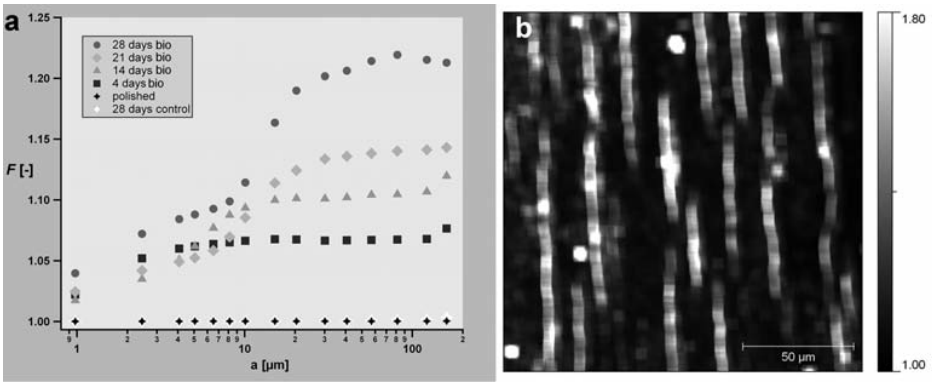

Figure 7: a) Evolution of *F* as function of the edge length of the squared sampling area calculated for fresh and reacted pyrrhotite surfaces. F at larger sampling size (>10 µm) is controlled by the deepening of 2C lamellae. b) Spatial distribution of *F* values for a squared sampling size with edge length *a*=4 µm. High *F* values (~1.6) can be found at the positions of the dissolved 2C lamellae. Since these areas represent only a small portion of the entire field of view, they are not detectable in the histogram. Very high *F* values originate from overlying particles (cf. Fig. 5), but they do not alter the converged roughness parameter determined from the histogram

peak-to-peak height S_z, the ten-point-height S_{10z}, the root-mean-square-gradient S_{dq}, the surface-skewness S_{sk}, the surface-kurtosis S_{ku}, and the surface area ratio F. The program uses freely selectable edge lengths for the desired sampling area, which is moved pixel by pixel over the entire field of view (cf. Fig. 5).

4.2. Evaluation of ROUGHNECK outputs

The surface area ratio, $F=A_{3D}/A_{2D}$, which describes the surface area of a three dimensional surface normalized by the two dimensional (projected) surface, is used as an example parameter to illustrate the statistical procedure. A perfectly flat surface will result in $F=1$, while a rough surface results in $F>1$. This parameter is a so-called hybrid surface parameter because it does not mainly depend on the amplitude but is more sensitive to the high frequency modulations of the surface as it is measured by the slope between adjacent surface points.

ROUGHNECK has been used to calculate the converged F parameters of the biologically dissolved pyrrhotite surface after 28 days (Fig. 5). The distribution of roughness parameters (here frequency *N* vs. *F*) can be plotted as histogram by applying discrete bins (Fig. 6a). The maxima of the distributions show the roughness value for a significant portion of the measured surface. For heterogeneous surfaces, a number of maxima may indicate various components with different surface roughness. In general, the maximum *F* value increases with increasing sampling area. At small scale (*a*=1 to 10 µm),

the first maxima represent only the roughness of the NC pyrrhotite matrix which dissolves slower than the 2C lamellae. At larger scale (*a*=15 to100 µm) the *F* value includes contributions from both because the spacing between the lamellae is smaller than the edge length of the sampling area.

The maxima of each distribution can be translated into a convergence graph plotting the *F* value of the maxima versus the sampling length *a*. Comparing predominant roughness values as a function of time allows to trace the increase in surface roughness of the NC matrix alone (*a*=1 to 10 µm) as well as the evolution of roughness for the entire surface (*a*=15 to100 µm). The output data for every sampling area can also be visualized providing a spatial roughness parameter distribution (Fig. 6b). This is particularly useful if certain surface components, like the locations of the former 2C lamellae, represent only a small portion of the entire surface and are hence not well represented in the histogram. From the roughness distribution image (*a*=4 µm) a roughness parameter for the 2C lamellae of 1.6 can be determined. In turn, this also validates that the roughness parameter distribution (Fig. 6a) is not sensitive for artefacts like overlying particles or inaccurately measured surface points.

5. The reaction pathway of secondary iron sulfide formation under anoxic condition: An experimental study on the reaction of lepidocrocite with dissolved sulfide

AMD waters are typically characterized by high amounts of ferric iron and sulphate. The formation of secondary iron sulfides in the subsurface is an important pathway to reduce the contaminant concentration and to raise the pH of overlying waters (*Bilek, 2006*). In this respect, the interaction between dissolved sulfide and ferric oxides can be regarded as a key reaction leading ultimately to pyrite formation (*Canfield et al., 1992, Poulton et al., 2004*), but knowledge on the pathways and on controlling factors is still limited. Here, results from batch experiments on the reaction between lepidocrocite and dissolved sulfide under anoxic conditions are presented with a special emphasis on the characterization of nanocrystalline products by TEM forming at different time steps.

5.1. Materials, experimental setup and methods

Kinetic batch experiments were conducted by mixing lepidocrocite (25 mmol/L) and different concentrations of dissolved sulfide at room temperature and a constant pH of 7 within an anoxic glove box. After 1-2 hours, 24 hours,

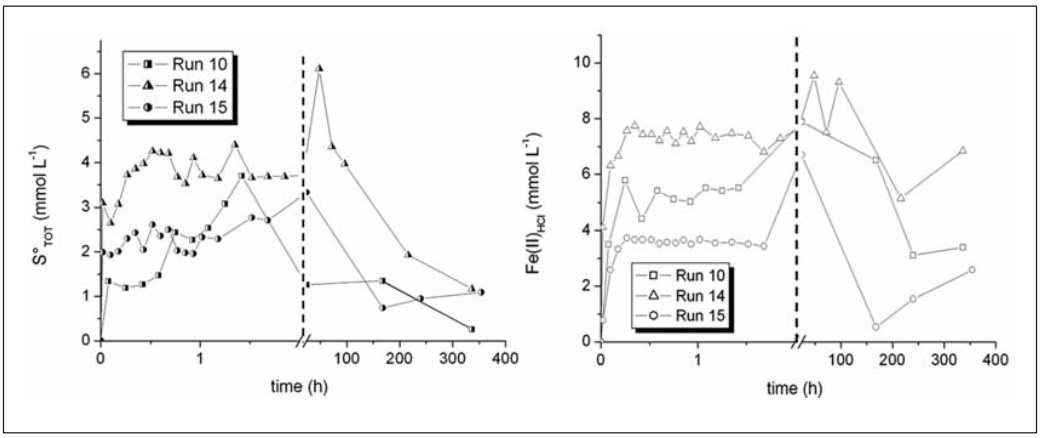

Figure 8: Evolution of elemental sulfur (left) and acid extractable ferrous iron (right) during two weeks of reaction for selected experimental runs. The initial sulfide concentration in run 10 and 14 was twice as the concentration in run 15. Mackinawite formation is rapid within the first hours of the experiments, whereas pyrite formation is relatively slow, starts after 2 days and continued to the end of the run

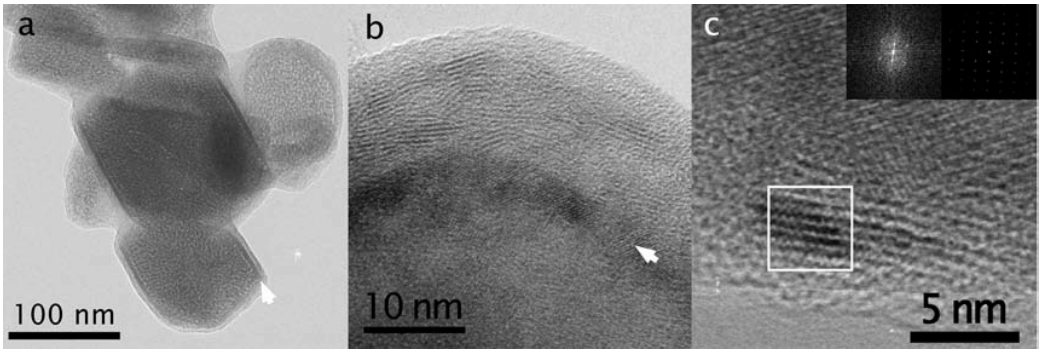

Figure 9: Bright field (a) and high resolution (b,c) TEM images of lepidocrocite crystals with sulfur-rich rims after 2 hours of reaction. The spotted contrast on lepidocrocite grains in (a) is due to nanocrystalline mackinawite. In (b) characteristic (001) and (111) lattice fringes of mackinawite (0.52 and 0.23nm, respectively) are visible in the outer rim. A continuous intermediate layer (arrow) shows fringes matching d_{220} of magnetite/maghemite (arrow). This layer can also be noticed in (a). A nanocrystal of mackinawite in [010] zone axis orientation is shown in (c) together with its calculated FFT and a simulated diffraction pattern as inset

1 week and 2 weeks, respectively, dissolved Fe(II) and S(-II), Fe(II) extractable with 0.5 N HCl, S°, and the total iron content were determined by wet chemistry extraction. At different time steps aliquots of the reacting suspension were analyzed by TEM, XRD and Mössbauer spectroscopy. In order to limit oxidation in air during TEM sample preparation the suspension was first sampled in gas-tight vials. A drop of solution was then taken with a syringe and put onto a Lacey carbon-coated copper grid. The grid was immediately transferred to the TEM holder and inserted into the high vacuum of the TEM. The short exposure of the sample to air can be limited to 1-2 minutes at maximum with this procedure.

5.2. Results

The reaction can be divided into three phases on the basis of wet chemistry (Fig. 8) and TEM observations (Figs. 9 and 10). In the first minutes of the reaction (0-15min) dissolved sulfide is rapidly consumed. It is partly oxidized to S° species in solution and partly consumed by initial mackinawite formation. In a second phase (15-120 min) a continuous but slower formation of S° is observed while acid extractable Fe(II) remained constant. TEM measurements revealed the occurrence of a mackinawite rim covering the lepidocrocite crystals that was separate from the lepidocrocite surface by an interfacial magnetite layer (Fig. 9). The magnetite layer can be seen as an intermediate stage linking two reactions, the formation of mackinawite which reduces ferric iron at the lepidocrocite surface on one hand and the transport of electrons in the deeper regions of the lepidocrocite bulk crystal which facilitates reductive dissolution and mackinawite rim growth and the other hand. The third phase is characterized by a decrease of acid extractable Fe(II) and S° and results in pyrite formation together with some magnetite (2-14 days). TEM measurements indicate that mackinawite completely dissolves from the surface of lepidocrocite while the precipitation of pyrite occurs separately from the lepidocrocite surface. The pyrite formation is coupled to mackinawite dissolution and probably accompanied by the formation of FeS clusters that serve as precursors. The conversion of mackinawite to pyrite was traced by TEM at 72 hours, 1 and 2 weeks. The mackinawite rims get gradually thinner and more corrugated with time. After 48 hours amorphous regions composed of iron and sulfur in variable concentration can be found between lepidocrocite grains. Pyrite grains reach diameters between 200 and 500 nm after 2 weeks and commonly show striking cubic or octahedral outlines (Fig. 10). However, the grains are composed of smaller cubic building blocks which point to a formation by oriented aggregation. In addition to pyrite, some magnetite grains similar in size and shape could be

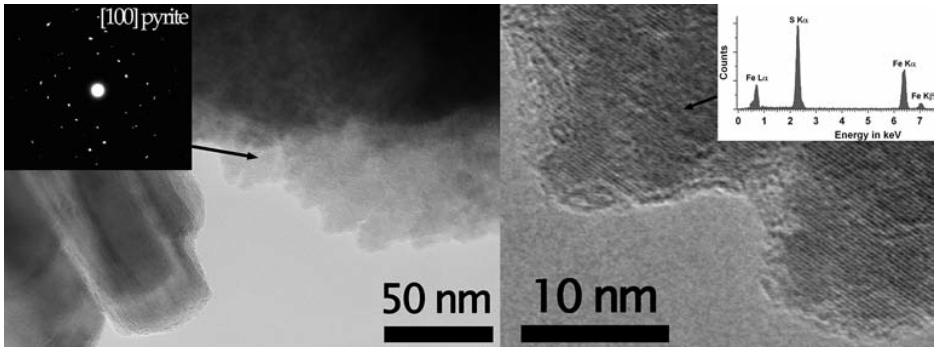

Figure 10: High resolution images, electron diffraction pattern and EDX spectra of pyrite. Note the aggregative nature of the grain consisting of cubic building blocks. Slight misorientations are also reflected in the diffraction pattern

identified by STEM-EDX and electron diffraction as well.

5.3. Discussion

The temporal evolution of the chemical species concentrations and solid phases indicate that the reaction progress is highly dynamic. TEM demonstrates that several phases form during the reaction towards pyrite. On the basis of the observed concentrations a number of balanced chemical equations can be formulated involving sorbed iron species as well as polysulfites. However, it is obvious that the system is kinetically controlled towards chemical equilibration (pyrite formation) due to the slow reductive dissolution process and the redox disproportionation. This study has provided novel insights into the redox processes occurring at the surface and in the vicinity of the lepidocrocite crystals and reveals the occurrence of magnetite and mackinawite in the initial phase of the reaction covering the lepidocrocite surface. It further demonstrates that dissolution of makkinawite occurs prior to formation of pyrite presumably being followed by further reaction with polysulfides in the absence of dissolved sulfide. It has also demonstrated that the kinetics of precursor formation from reductive dissolution of ferric (hydr)oxides by hydrogen sulfide and of subsequent pyrite formation are kinetically decoupled. This observation implies that in iron-rich aqueous systems of periodical sulfide formation (e.g. movement of the capillary fringe in ground waters) ferric oxides may undergo »charging« with reduced substances that may lead to pyrite (and magnetite) formation even in the absence of dissolved sulfide. This reactions sequence has also implications for the retention of toxic metal by adsorption on nanocrystalline mackinawite which may get mobilized by further reaction to pyrite.

6. Conclusion

The most important scientific insights obtained within the MIMOS project are:

(i) A new structural model (TIM model) has been successfully applied to non-stoichiometric NC-pyrrhotite. It well explains important structural details that are observed in electron diffraction patterns and dark-field images and can lead to a better understanding of surface and bulk physical properties of pyrrhotite relevant to geomagnetics, petrology, environmental mineralogy, and technical mineral processing.

(ii) Differences in reactivity caused by small structural and chemical variations have been directly proven for biologically-enhanced dissolution of pyrrhotite. The intergrowth texture has therefore a direct influence on the dissolution rate by a continuous increase of reactive surface area. This result is relevant for the assessment of the weathering rates of pyrrhotite tailings and bioleaching applications.

(iii) The evolution of surface area was quantified by combining topographic data and a

statistical evaluation of surface roughness using the newly developed program ROUGHNECK for heterogeneous surfaces. This approach provides new prospects for mineral dissolution studies as well as for more general topics dealing with surface alteration like corrosion.

(iv) Analytical TEM was successfully applied to tracing the reaction pathway of iron sulfide formation. The new results are relevant for our understanding of processes and element distributions at geochemical boundaries which can help to decipher successful remediation strategies for polluted waters and soils.

References

Amelinckx, S. & Van Dyck, D. (1992) Electron diffraction effects due to modulated structures. Electron diffraction techniques, IUCr/Oxford Science Publications, 2, 309-373.

Asta, M.P., Cama, J., Soler, J.M., Arvidson, R.S. & Lüttge, A. (2008) Interferometric study of pyrite surface reactivity in acidic conditions. Am. Mineral., 93, 508-519.

Becker, M., de Villiers, J. & Bradshaw, D. (2010) The flotation of magnetic and non-magnetic pyrrhotite from selected nickel ore deposits. Miner. Eng., in press, doi:10.1016/j.mineng.2010.07.002

Belzile, N., Chen Y., Cai, M. & Li, Y. (2004) A review on pyrrhotite oxidation. Journal of Geochemical Exploration, 84, 65-76.

Blunt, L. & Stout, K.J. (2001) EC Project Final Report »Development of a Basis for 3D Surface Roughness Standards« SMT4-CT98-2209.

Bilek, F. (2006) Column tests to enhance suphide precipitation with liquid organic electron donators to remediate AMD-influenced groundwater. Environ. Geol., 49, 674-683.

Canfield D. E., Raiswell R. & Bottrell S. (1992) The reactivity of sedimentary iron minerals toward sulphide. Am. J. Sci., 292, 659-683.

Church, C.D., Wilkin, R.T., Alpers, C.A., Rye, R. O. & McCleskey, R.B. (2007) Microbial sulfate reduction and metal attenuation in pH 4 acid mine water. Geochem. Transac., doi:10.1186/1467-4866-8-10.

Ekmekçi, Z., Becker, M., Bagci Tekes, E. & Bragshaw, D. (2010) An impedance study of the adsorption of CuSO4 and SIBX on pyrrhotite samples of different provenances. Miner. Eng., in press, doi:10.1016/j.mineng.2010.02.007

Fischer, C. & Lüttge, A. (2007) Converged surface roughness parameters – A new tool to quantify rock surface morphology and reactivity alteration. Am. J. Sci. 2007, 307, 955-973.

Gehrke, T., Telegdi, J., Thierry, D. & Sand, W. (1998) Importance of extracellular polymeric substances from Thiobacillus ferrooxidans for bioleaching. Appl. Environ. Microbiol., 64, 2743 – 2747.

Izaola, Z., Gonzalez, S., Elcoro, L., Perez-Mato, J.M., Madariaga, G. & Garcia, A. (2007) Revision of pyrrhotite structures within a common superspace model. Acta Cryst. B, 63, 693-702.

Janzen, M.P., Nicholson, R.V. & Scharer, J.M. (2000) Pyrrhotite reaction kinetics: reaction rates for oxidation by oxygen, ferric iron, and for nonoxidative dissolution. Geochim. Cosmochim. Acta 64, 1511 –1522.

Jiang, L., Zhou, H.Y. & Peng, X.T. (2007) Biooxidation of pyrite, chalcopyrite and pyrrhotite by Acidithiobacillus ferrooxidans. Chin. Sci. Bull., 52, 2702-2714.

Ke, J. & Li, H. (2006) Bacterial leaching of nikkel-bearing pyrrhotite. Hydrometallurgy, 82, 172-175.

Legrand, D.L., Bancroft, G.M. & Nesbitt, H.W. (1995) Oxidation/alteration of pentlandite and pyrrhotite surfaces at pH 9.3: Part 1. Assignment of XPS spectra and chemical trends. Am. Min., 90, 1042-1054.

Morimoto, N., Gyobu, A., Tsukuma, K. & Koto, K. (1975) Superstructure and nonstoichiometry of intermediate pyrrhotite. Am. Min., 60, 240-248.

Nakazawa, H. & Morimoto, N. (1970) Pyrrhotite phase relations below 320°C. Proc. Japan Acad., 46, 678-683.

Nicholson, R.V. & Scharer, J.M. (1994): Laboratory studies of pyrrhotite oxidation kinetics. In: Environmental geochemistry of sulfide oxidation. Alpers C.N., Blowes D.W. (eds.), .ACS Symp. Series 550, 14-30.

Ohfuji, H. & Rickard, D. (2006) High resolution transmission electron microscopic study of synthetic nanocrystalline mackinawite. Earth and Planetary Science Letters, 241, 227-233.

Pierce, L. & Buseck, P.R. (1974) Electron imaging of pyrrhotite superstructures. Science, 186, 1209-1212.

Pollok, K., Langenhorst, F., Hopf, J., Kothe, E., Geisler, T., Putnis, C.V. & Putnis, A. (2008) Microstructural Controls on Monosulfide Weathering and Heavy Metal Release (MIMOS), GEOTECHNOLOGIEN Science Report, 12, 79-88.

Poulton S.W., Krom, D.M. & Raiswell R. (2004) A revised scheme for the reactivity of iron (oxyhydr)oxide minerals towards dissolved sulfide. Geochim. Cosmochim. Acta, 68, 3703-3715.

Rawlings, D.E. (2002) Heavy metal mining using microbes. Annual Reviews in Microbiology, 56, 65–91.

Rodriguez, Y., Ballester, A., Blazquez, M. A. & Munoz, J. A. (2003) Study of bacterial attachment during the bioleaching of pyrite, chalcopyrite and sphalerite. Geomicrobiol. J. 20, 131–141.

Rodriguez-Leiva, M. & Tributsch, H. (1988) Morphology of bacterial leaching patterns by Thiobacillus ferrooxidans on synthetic pyrite. Arch. Microbiol. 149, 401–405.

Sand W., Gehrke, T., Hallman, R. & Schippers, A. (1995) Sulfur chemistry, biofilm, and the (in)direct attack mechanism – a critical evaluation of bacterial leaching. Appl. Microbiol. Biotechnol., 43, 961-966.

Schippers, A. (2004) Biogeochemistry of metal sulfide oxidation in mining environments, sediments and soils. In:Amend, J.P., Edwards, K.J., Lyons, T.W. (Eds.), Sulfur Biogeochemistry—Past and Present. Special Paper, vol. 379. Geological Society of America, Boulder, Colorado, pp. 49-62.

Schippers, A., Kock, D., Schwartz, M., Böttcher, M.E., Vogel, H. & Hagger, M. (2007) Geomicrobiological and geochemical investigation of a pyrrhotite-containing mine waste tailings dam near Selebi-Phikwe in Botswana. J. Geochem. Expl., 92, 151-158.

Yamamoto, A. & Nakazawa, H. (1982) Modulated structure of the NC-type (N = 5.5) pyrrhotite, Fe1-xS. Acta Cryst. A, 38(1), 79-86.